



# Surfactants assisted SnO<sub>2</sub> nanoparticles synthesized by a hydrothermal approach and potential applications in water purification and energy conversion

S. Suthakaran<sup>1</sup> · S. Dhanapandian<sup>1</sup> · N. Krishnakumar<sup>1</sup> · N. Ponpandian<sup>2</sup>

Received: 22 March 2019 / Accepted: 10 June 2019 / Published online: 15 June 2019  
© Springer Science+Business Media, LLC, part of Springer Nature 2019

## Abstract

SnO<sub>2</sub> nanoparticles (NPs) were synthesized by facile hydrothermal method in the presence of polyethylene glycol (PEG), cetyl trimethylammonium bromide (CTAB) and sodium hexametaphosphate (SHMP) as surfactant. The synthesized samples were characterized by X-ray powder diffraction (XRD), Fourier transform infrared spectroscopy (FTIR), high resolution scanning electron microscopy (HRSEM), high resolution transmission electron microscopy (HRTEM), selected area electron diffraction (SAED), UV–visible diffuse reflectance spectroscopy (UV–visible DRS) and photoluminescence (PL). The XRD studies revealed that the position of diffraction peaks agreed well with the reflection of a tetragonal structure of SnO<sub>2</sub> phase. The structure of the SnO<sub>2</sub> did not change by introducing surfactants but the crystallite size was decreased. The optical studies revealed a clear blue shift in the band gap energy (E<sub>g</sub>) with a decrease in particle size. The PL intensity of SHMP assisted NPs is lower than that of bare SnO<sub>2</sub> and other surfactant assisted SnO<sub>2</sub> NPs, which indicated the suppression of the recombination of the photogenerated carriers. These results reveal that SHMP assisted SnO<sub>2</sub> NPs is suitable for further electrochemical and photocatalytic activity. The surfactant (SHMP) assisted SnO<sub>2</sub> photocatalyst exhibited the increased photocatalytic activities compared with the bare SnO<sub>2</sub> photocatalyst. Furthermore, the SHMP assisted SnO<sub>2</sub> electrode exhibited the increased supercapacitor performances.

## 1 Introduction

Past few years, the major problem is the environmental pollution through the water contamination and energy deficiency. To over this problem, the contamination in waste water from the industries should be removed and also develop high and large power density energy storage devices to solve many environmental issues. In the recent years, supercapacitors (SCs)/electrochemical capacitors (ECs) have become popular energy storage devices because they can produce a huge amount of energy in a short span of period and large power density. They have excellent cyclability and extraordinary performance compare to fuel cells and commercial batteries [1–5].

The waste water from industries have contaminated various organic and metallic ions. High toxic dyes are used in different industries like textile, dying, biomedical and food-stuff. The water is contaminated by the waste water from these industries. These contaminants result in a high biochemical oxygen demand (BOD), high chemical oxygen demand (COD), bad smell, toxicity and exceed the tolerance limits in water. Hence, the dyes must be completely removed from industrial waste water. Recently, photocatalysts have been proposed as an alternative to the conventional approaches to eliminate the contamination from the industrial waste water. Dye molecules are converted into non-hazardous compounds by the photodegradation process. Therefore, efforts are taken to establish novel metal oxide semiconductor photocatalysts for the degradation of such organic pollutants [6–10].

The engineering of inorganic semiconducting nanostructures attracts interest in various fields by their unique properties such as, structural, optical, magnetic electronic and catalytic, which differs significantly from those of their bulk counterparts. Recent researches targeted on the synthesis and characterization of semiconductor nanostructures

✉ S. Dhanapandian  
professordhana10@gmail.com

<sup>1</sup> Department of Physics, Annamalai University,  
Annamalainagar, Chidambaram, Tamilnadu 608 002, India

<sup>2</sup> Department of Nanoscience and Technology, Bharathiar  
University, Coimbatore, Tamilnadu 641 046, India

with well defined morphologies and accurately tunable size. These act as promising agents for energy and environmental applications like, lithium-ion battery, Microwave absorbing materials, photocatalytic water splitting for hydrogen production, sensors, dye-sensitized solar cells and photocatalytic remediation of organic pollutants from air and water [11–19].

Several semiconductors such as,  $\text{MnO}_2$ ,  $\text{TiO}_2$ ,  $\text{V}_2\text{O}_5$ ,  $\text{Fe}_2\text{O}_3$ ,  $\text{CdS}$  and  $\text{SnO}_2$  are deeply explored as novel electrode materials for electrochemical as well as photocatalytic applications because of their special architecture and high catalytic activities [20–28]. Among the various semiconductors,  $\text{SnO}_2$  has attracted material owing due to its abundance, non-toxicity, low cost, harmless and outstanding physical and chemical properties and also it has great flexibility in structure and morphology.  $\text{SnO}_2$  is a typical n-type semiconductor with a band gap energy ( $E_g$ ) of 3.6 eV. This is mainly used in gas sensors [29, 30], dye-based solar cells [31], rechargeable lithium batteries [32], transparent conducting electrode [33], optoelectronic devices [34], photocatalytic application [35, 36] and energy storage devices [37, 38]. In this regard, several approaches are proposed to increase the electrochemical performance and photocatalytic activity by synthesizing the desired nanostructures by reducing the crystalline size and preventing agglomeration. Hence, the surfactant molecules are used to provide electronic and chemical passivation of the surface dangling bonds. They arrest agglomeration and uncontrolled growth of the NPs. Further, these capping molecules permit chemical manipulations of the NPs similar to that of large molecules which have their solubility and reactivity determined by the nature of the surface ligands. It is well clear that surfactants have the ability to change the intrinsic properties of materials and to enhance the electrochemical and photocatalytic activity.

To synthesis  $\text{SnO}_2$  NPs, different methods like co-precipitation, sputtering, green synthesis, microwave heating method, chemical vapor deposition, spray pyrolysis, pulsed laser deposition and hydrothermal methods are used [39–44]. Among them, hydrothermal method is chosen for the present work because of non-polluting, saves energy and easy control size and morphology. In this method, the oxygen vacancies are generated in  $\text{SnO}_2$  NPs and these can instigate the formation of new energy levels in the band gap. When  $\text{Sn}(\text{OH})_4$  is heated the hydroxyls remain in the same structure and will generate more water, when the lattice oxygen is released. It position has neutral vacancy. Moreover, in the hydrothermal process high pressure is generated and it is favorable to remove hydroxyls and producing oxygen vacancies. The insoluble species are dissolved or recrystallized in a high-pressure atmosphere. The rate of chemical reaction in the hydrothermal process is faster since it has smaller crystallite size and subsequently a higher electrochemical and photocatalytic activity.

In this work,  $\text{SnO}_2$  NPs with reduced crystallite size have been successfully synthesized through facile hydrothermal method using non-ionic surfactant PEG, cationic surfactant CTAB and anionic surfactant SHMP. The size, morphology and optical properties of  $\text{SnO}_2$  NPs are studied by the influence of surfactants. In the present work, SHMP assisted  $\text{SnO}_2$  NPs are used for the degradation of methyl violet (MV) dye. Further, the electrochemical performance of SHMP assisted  $\text{SnO}_2$  NPs are found to be suitable as supercapacitor electrode materials.

## 2 Materials and methods

### 2.1 Materials

Tin (IV) chloride pentahydrate ( $\text{SnCl}_4 \cdot 5\text{H}_2\text{O}$ ), sodium hydroxide (NaOH), polyethylene glycol, cetyl trimethylammonium bromide, and sodium hexametaphosphate were selected as starting materials. All chemical reagents were analytical graded with 99.99% so further purification was not necessary. Distilled water was used for the synthesis of  $\text{SnO}_2$  NPs.

### 2.2 Synthesis of bare and surfactants (PEG, CTAB and SHMP) assisted $\text{SnO}_2$ NPs

For the synthesis of  $\text{SnO}_2$  NPs, 0.26 M  $\text{SnCl}_4 \cdot 5\text{H}_2\text{O}$  was dissolved in 50 ml of distilled water. Subsequently 1.30 M NaOH pellets were dissolved in 50 ml of distilled water and it was added drop wise into 50 ml of  $\text{SnCl}_4$  solution and a white precipitate was formed. This was stirred continuously for 45 min to obtain homogeneous solution. In a similar manner, surfactant assisted  $\text{SnO}_2$  NPs were synthesized by treating 1 g of nonionic surfactant (PEG), 1 g of cationic surfactant (CTAB) and 1 g of anionic surfactant (SHMP) was added drop wise into the above mixture and stirred for another half an hour to form a homogeneous solution. Further, the above solutions were shifted to 150 ml autoclave made of Teflon-lined stainless steel. The sealed autoclave was kept in the oven and maintained at 160 °C for 12 h and then cooled naturally at room temperature. After reaction, the resulting products were filtered by washing thoroughly with ethanol and distilled water to remove moisture and then collected. Finally, the samples were dried at 100 °C for 6 h, followed by calcinations at 500 °C for 3 h to get the final bare and surfactant assisted  $\text{SnO}_2$  NPs.

### 2.3 Characterization techniques

The crystalline structure and crystallite sizes of the samples were studied by recording using XRD (X'PERT PRO diffractometer) with  $\text{Cu K}\alpha$  radiation of wavelength 1.5418 Å.

The chemical bonding existing in samples were recorded with RX I Perkin Elmer FTIR spectrometer over a wave number range from 4000 to 400  $\text{cm}^{-1}$ . The morphology of the samples was monitored by a HRSEM (FET Quanta FEG 200 spectrometer) and HRTEM (JEM-2100). The optical properties were determined using UV–Vis DRS (VARIAN Carry 5000) in the wavelength ranging from 300 to 700 nm. The emission spectra of the samples were recorded with the help of a Jobin–Yvon, FLUOROLOG-FL3-11 spectrofluorometer.

## 2.4 Photocatalytic experiments

The photocatalytic activity of bare  $\text{SnO}_2$  and SHMP assisted NPs for the degradation of MV was examined under sunlight irradiation. In this experiment, 5 mg of  $\text{SnO}_2$  photocatalyst was dispersed in 200 ml of aqueous suspensions of MV with an initial concentration of  $1 \times 10^{-4} \text{ mol L}^{-1}$  for irradiation experiments. The suspension mixture was stirred in the dark for about 30 min prior to irradiation, to achieve good dispersion and reach an adsorption–desorption equilibrium between methyl violet dye and catalytic surface. The suspension mixture was then exposed to sunlight irradiation and stirred continuous. Five milliliters aliquot was withdrawn through a pipette for every 10 min from a reaction mixture. Before analyzing, to remove solid catalyst particles the suspension was centrifuged. Degradation of organic dye was investigated by using UV–visible spectrometer (VARIAN Carry 5000) at different time intervals. The experiment processes was taken place on a sunnyday (April) at Annamalainagar, Tamilnadu between 11 a.m–2 p.m (outside temperature 35 °C to 40 °C).

## 2.5 Electrochemical performance

The electrochemical performance of the bare  $\text{SnO}_2$  and SHMP assisted NPs were examined in an electrochemical analyzer (Versa STAT Princeton Applied Research – AMETEK model) using three-electrode system containing Platinum foil as a counter electrode, Ag/AgCl as a reference electrode and  $\text{SnO}_2$  as a working electrode. The series of experiments were carried out in 6 M KOH as an electrolyte. The electrochemical performance was evaluated by using cyclic voltammetry (CVs), galvanostatic charge/discharge (GCD) and electrochemical impedance spectroscopy (EIS).

## 3 Results and discussion

### 3.1 Structural analysis

The powder XRD helps to identify the phase structure and purity of the  $\text{SnO}_2$  NPs. Figure 1 represents the XRD patterns

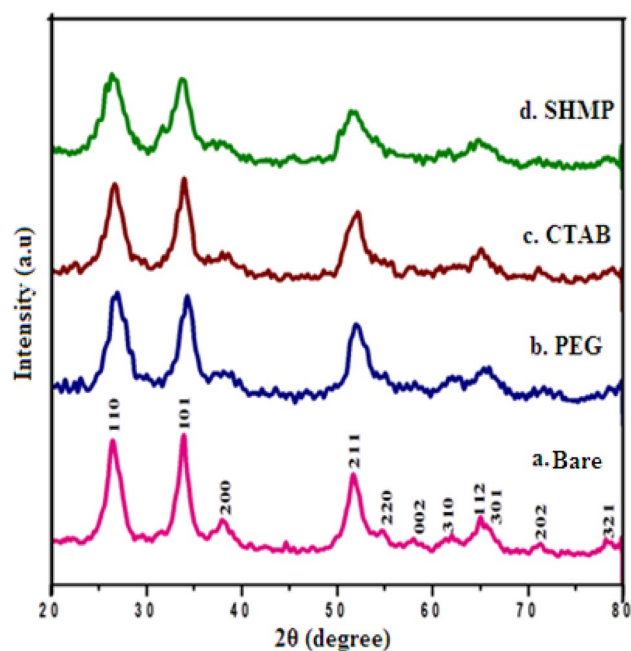


**Fig. 1** XRD pattern of synthesized  $\text{SnO}_2$  nanoparticles a Bare, b PEG assisted, c CTAB assisted and d SHMP assisted

of the bare and surfactant assisted  $\text{SnO}_2$  NPs. Both (bare and surfactant assisted  $\text{SnO}_2$ ) NPs exhibit a similar XRD patterns that can be assigned to tetragonal structure of  $\text{SnO}_2$  with lattice constant of  $a=b=4.738$  and  $c=3.187$  (JCPDS card number 41-1445) [45]. The absence of additional peaks in the XRD results confirms that the synthesized NPs have high phase purity. The diffraction peaks of surfactants assisted  $\text{SnO}_2$  samples are quite broad due to the small crystallite size. From the XRD data, average crystallite sizes of the both NPs can be calculated using the Scherrer equation [46, 47].

$$D = \frac{k\lambda}{\beta \cos\theta} \quad (1)$$

where  $D$  is the crystallite size,  $k$  is the shape factor,  $\lambda$  is the wavelength of the X-ray ( $\lambda = 1.5406 \text{ \AA}$ ),  $\beta$  is the full width at half maximum (FWHM) of the peak and  $\theta$  is the angle of the diffraction. The lattice parameters for tetragonal structure  $\text{SnO}_2$  NPs are calculated from the following equation [48].

$$\frac{1}{d^2} = \left( \frac{h^2 + k^2}{a^2} \right) + \left( \frac{l^2}{c^2} \right) \quad (2)$$

where  $a$  and  $c$  are the lattice constants  $h$ ,  $k$  and  $l$  are the miller indices. Dislocation density ( $\delta$ ) is determined by using following relation [49].

$$\delta = \frac{1}{D^2} \quad (3)$$

The micro strain ( $\epsilon$ ) can be calculated using the formula [48]

$$\epsilon = \frac{\beta \cos \theta}{4} \quad (4)$$

All calculated values are presented in Table 1.

The crystallite size of bare SnO<sub>2</sub> NPs is found to be about 5.3 nm. Further, the crystallite size of PEG, CTAB and SHMP assisted SnO<sub>2</sub> NPs are calculated using Eq. (1) are 4.44, 4.31 and 3.33 nm, respectively. Hence, the XRD results reveal that the crystallite size of SnO<sub>2</sub> NPs can be tuned by adding surfactants as capping agents. The above equations are used to evaluate the crystallite size, dislocation density, lattice parameters and micro strain of the synthesized SnO<sub>2</sub> NPs and it is given in Table 1. In addition, it can be seen that the dislocation density and micro strain increase with respect to adding surfactants. Hence, from the XRD studies it is confirmed that the crystallite size of the NPs can be reduced by introducing surfactants.

### 3.2 Functional group analysis

FTIR spectroscopy is a vibrational spectroscopic technique, which is used to investigate the presence of functional groups of the samples. The FTIR spectra of both NPs are recorded in the range of 4000 to 400 cm<sup>-1</sup> and are presented in Fig. 2. As seen from the FTIR spectra, the appearance of broad absorption band around 3415 cm<sup>-1</sup> is assigned to the O–H stretching vibration of surface hydroxyl groups [50]. The weak absorption band around 2978 cm<sup>-1</sup> indicated the presence of asymmetric stretching vibrations of C–H bond [50–52]. The band around 1570 cm<sup>-1</sup> is ascribed to the stretching vibration of C=C [53]. The absorption bands located in the region 1420–1400 cm<sup>-1</sup> are attributed to the asymmetric and symmetrical stretching vibrations of C–O because of the COOH groups. The medium absorption band located around 1020 cm<sup>-1</sup> is assigned to the C–O–C symmetrical stretching vibration [54]. The characteristics observed below 800 cm<sup>-1</sup> is very important because they indicate the presence of Sn–O bands and their functional group. The sharp and broad absorption band noticed around 650 cm<sup>-1</sup> is attributed to lattice mode of SnO<sub>2</sub> and the

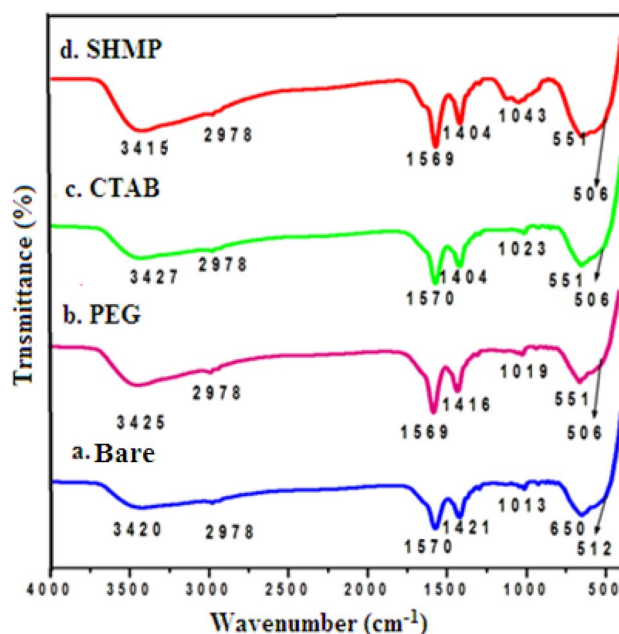


Fig. 2 FTIR spectra of synthesized SnO<sub>2</sub> nanoparticles a Bare, b PEG assisted, c CTAB assisted and d SHMP assisted

infrared band located around 510 cm<sup>-1</sup> is associated with the Sn–O stretching vibration [55–57]. None of the bands are seen in the spectra except metal and oxygen functional groups.

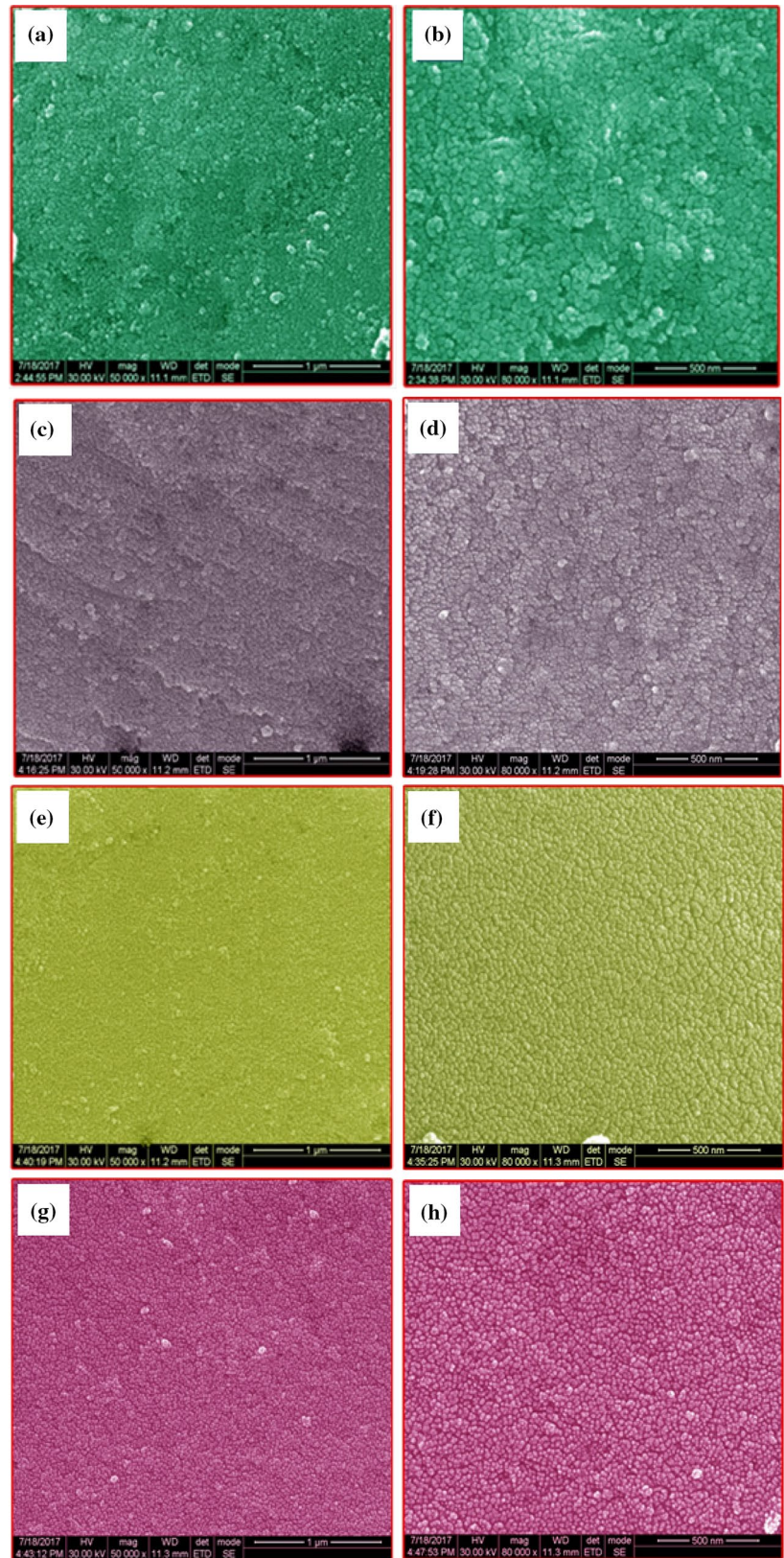
### 3.3 Morphological studies

The morphology of the SnO<sub>2</sub> NPs are investigated by HRSEM. Figure 3 depicts the HRSEM images of the both NPs. As seen in the Fig. 3a, b the agglomerated spherical like morphologies are observed in the low and high magnification of the bare SnO<sub>2</sub> NPs. However, from the HRSEM images (Fig. 3c–h), it is evident that well-dispersed spherical NPs are observed in the surfactants assisted NPs. These results clearly reveal that the surfactants do not involve in changing the shape of the SnO<sub>2</sub> NPs but influence in reducing the crystallite size and arrest the agglomeration of the particles.

**Table 1** Structural parameters of bare and surfactant assisted SnO<sub>2</sub> nanoparticles

Surfactant	Crystallite size (nm)	Dislocation density ( $\delta$ ) $\times 10^{14}$ lines/m <sup>2</sup>	Lattice parameters ( $\text{\AA}$ )		Micro strain ( $\epsilon$ ) $\times 10^{-3}$
			a=b	c	
Without surfactant	5.3	355.9	4.739	3.189	6.517
PEG	4.44	507.2	4.728	3.184	7.866
CTAB	4.31	538.3	4.723	3.159	8.080
SHMP	3.33	901.8	4.750	3.193	10.502

**Fig. 3** HRSEM images of synthesized SnO<sub>2</sub> nanoparticles **a, b** Bare, **c, d** PEG assisted, **e, f** CTAB assisted and **g, h** SHMP assisted



### 3.4 TEM analysis

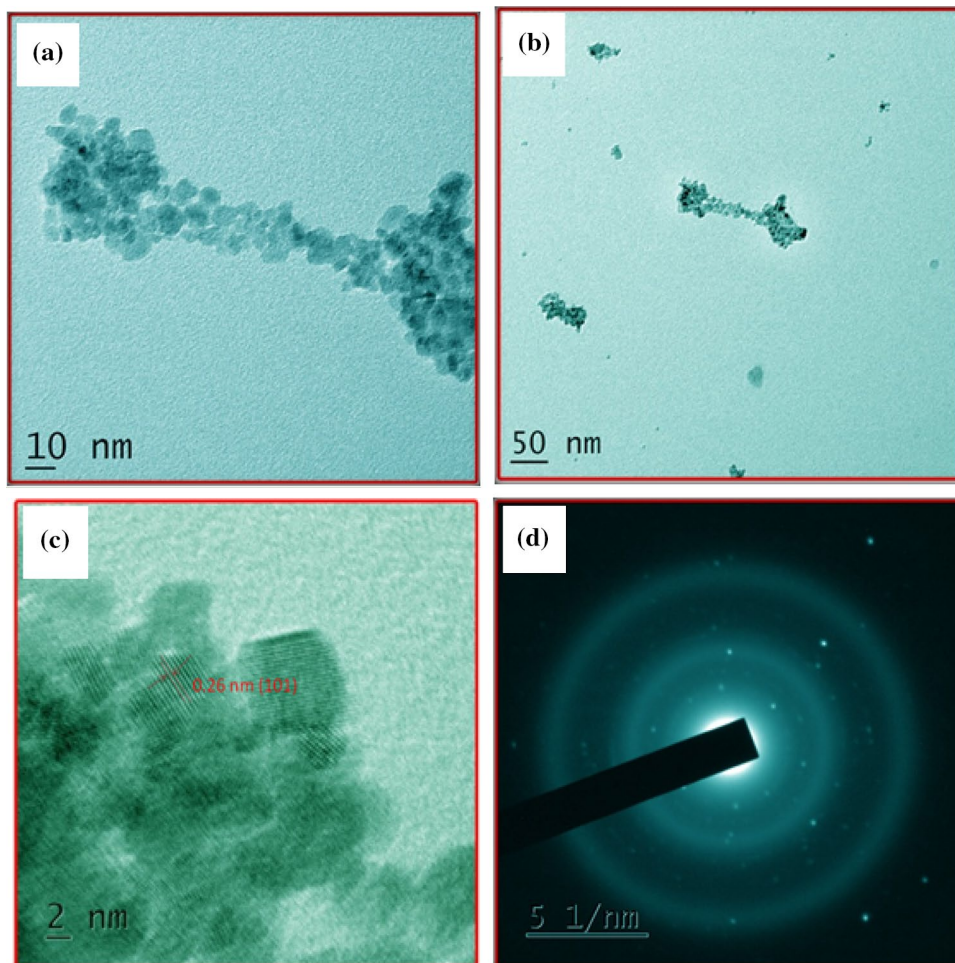
The morphology and average particle size of the bare SnO<sub>2</sub> NPs can be depicted from the TEM images. By using HRTEM the microstructure of the bare SnO<sub>2</sub> NPs is examined. The HRTEM image and SAED pattern of the bare SnO<sub>2</sub> NPs are shown in Fig. 4c and d. From the TEM images (Fig. 4a, b), it is clearly seen that spherical structured SnO<sub>2</sub> NPs are formed. It is well accordant with the HRSEM images. The lattice spacing is calculated from the HRTEM image and found to be 0.26 nm which corresponds to (101) lattice plane [59]. The SAED pattern indicates that the synthesized bare SnO<sub>2</sub> NPs are polycrystalline in nature. The diffraction ring in Fig. 4d corresponds to the (110), (101), (200) and (211) lattice planes for tetragonal structure of SnO<sub>2</sub> [58]. The SAED patterns match well with the XRD results. The size distribution histogram is clearly shown in Fig. 8a and the particle size is found to be 5.93 nm.

Figure 5 shows the TEM, HRTEM and SAED patterns of the PEG assisted SnO<sub>2</sub> NPs. TEM images (Fig. 5a–b) show the spherical like SnO<sub>2</sub> NPs, which coincides with the obtained HRSEM images. The lattice spacing is calculated

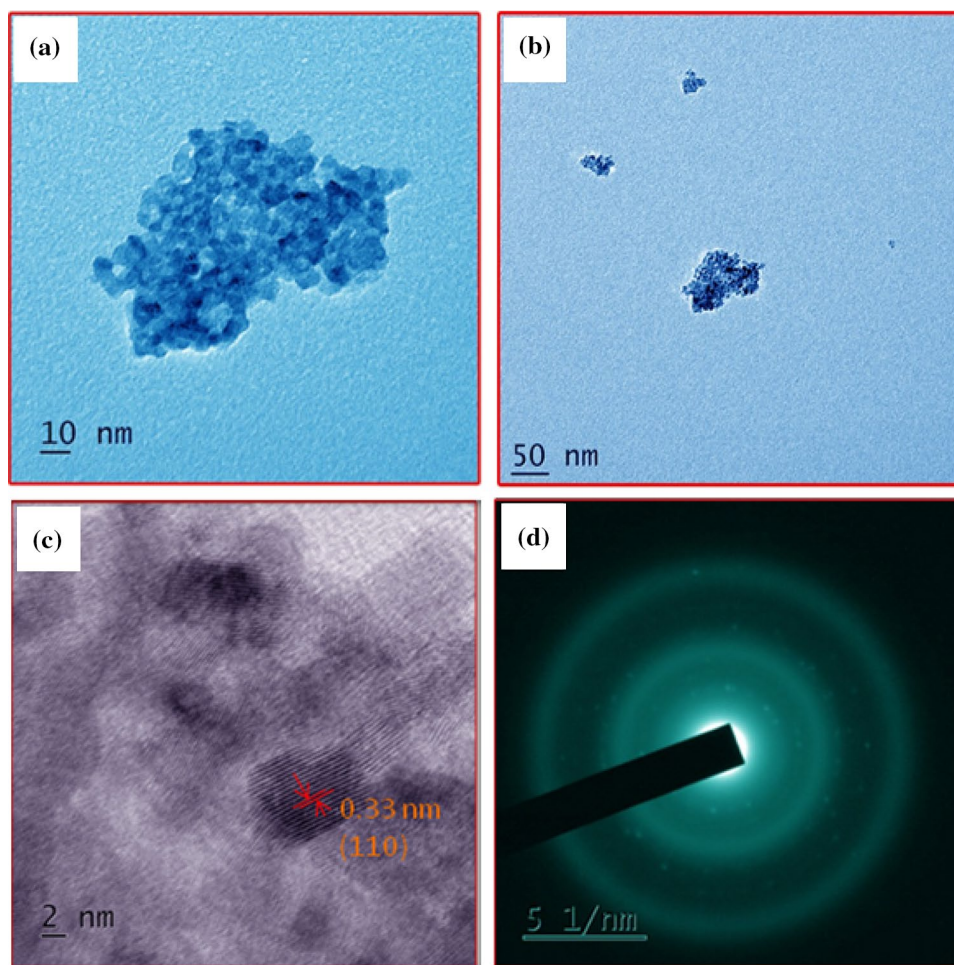
from the HRTEM image (Fig. 5c) and it is found to be 0.33 nm which correspond to (110) lattice plane of SnO<sub>2</sub> [60]. The SAED patterns of the SnO<sub>2</sub> NPs show defined rings, which could be attributed to the polycrystalline nature of PEG assisted SnO<sub>2</sub> NPs. The diffraction ring in Fig. 5d corresponds to the lattice plane (110), (101), (200) and (211), respectively [59]. Further, the particle size distribution histogram is clearly shown and the particle size is found to be 4.03 nm (Fig. 5b).

Figure 6 shows the TEM, HRTEM and SAED patterns of the CTAB assisted SnO<sub>2</sub> NPs. From the TEM images (Fig. 6a, b), it can be clearly seen that spherical structures of SnO<sub>2</sub> NPs are formed. The similar morphology is also obtained from the HRSEM images. From the HRSEM images the distances of the lattice fringes can be calculated and it is shown in Fig. 6c. They are found to be 0.33 nm, which corresponds to (110) lattice plane [60]. The SAED patterns of SnO<sub>2</sub> NPs with CTAB show well defined rings, which demonstrate the polycrystalline nature of synthesized SnO<sub>2</sub> NPs. The diffraction ring in Fig. 6d corresponds to the lattice plane (110), (101), (200) and (211), respectively [58]. The particle size can be calculated from the TEM images

**Fig. 4** a and b TEM images of synthesized bare SnO<sub>2</sub> nanoparticles, c HRTEM images of synthesized bare SnO<sub>2</sub> nanoparticles and d SAED pattern of synthesized bare SnO<sub>2</sub> nanoparticles



**Fig. 5** **a** and **b** TEM images of synthesized PEG assisted SnO<sub>2</sub> nanoparticles, **c** HRTEM images of synthesized PEG assisted SnO<sub>2</sub> nanoparticles and **d** SAED pattern of synthesized PEG assisted SnO<sub>2</sub> nanoparticles



and are shown in the Fig. 8c. The size distribution histogram shows the mean diameter of 4.22 nm.

Figure 7a, b and d shows the TEM images and SAED pattern of SHMP assisted SnO<sub>2</sub> NPs. The large quantities of uniformly sized and well dispersed spherical NPs are observed. The similar morphology is obtained from the HRSEM images. In Fig. 7c, HRTEM images of the spherical NPs are depicted. From the HRTEM images the lattice spacing of the NPs can be calculated. They are found to be 0.21 and 0.23 nm, which corresponds to (210) and (200) lattice planes, respectively. The SAED pattern reveals a polycrystalline nature of the SnO<sub>2</sub> NPs and diffraction rings can be indexed as (110), (101), (200) and (211) planes [58]. The particle size can be calculated from the TEM images and are shown in the Fig. 8d. The size distribution histogram clearly shown that the particle size is 3.60 nm. Hence, it is clearly seen that the surfactants are introduced as capping agents to decrease the particle size of SnO<sub>2</sub> NPs. Furthermore, the particle size of SnO<sub>2</sub> NPs are formed by using anionic surfactant (SHMP) and it is smaller than that of SnO<sub>2</sub> NPs formed by using non-ionic (PEG) and cationic surfactant (CTAB). Moreover, the results obtained from TEM images

and SAED patterns are in excellent agreement with the XRD results.

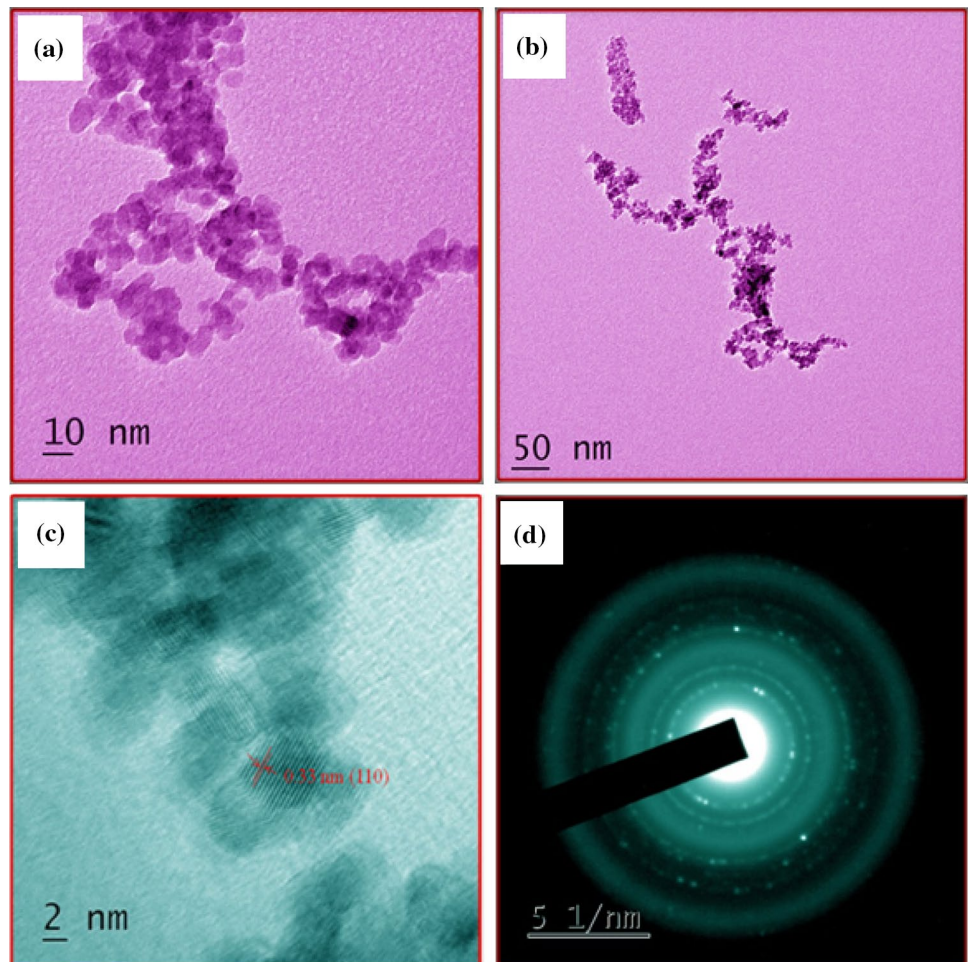
### 3.5 Optical properties

In order to investigate the optical properties, the reflectance spectra of the both NPs are recorded in the range of 200–800 nm and are shown in Fig. 9. As seen from the Fig. 9a–d it is apparent that all the synthesized products have exhibited a good optical quality in the visible region since the complete reflectance obtained in the range of around 400 nm. However, the absorption edges of the surfactants assisted SnO<sub>2</sub> NPs exhibit an obvious blue shift and this suggests an increase of the energy band gap. This result further indicates the decrease in particle sizes of surfactants assisted SnO<sub>2</sub> NPs.

The Eg can be calculated by the Kubelka–Munk function [61]

$$F(R) = \frac{(1 - R)^2}{2R} \quad (5)$$

**Fig. 6** **a** and **b** TEM images of synthesized CTAB assisted SnO<sub>2</sub> nanoparticles, **c** HRTEM images of synthesized CTAB assisted SnO<sub>2</sub> nanoparticles and **d** SAED pattern of CTAB assisted synthesized SnO<sub>2</sub> nanoparticles



where  $F(R)$  is the Kubelka–Munk function, which corresponds to absorbance and  $R$  is reflectance of the samples. The band gap energy ( $E_g$ ) of both NPs are estimated by extrapolating of the linear portion of the  $(F(R) \times h\nu)^{1/2}$  versus  $h\nu$  and are shown in Fig. 10a–d. The band gap energy has been found to be 3.92, 3.93, 3.94 and 3.95 eV for the sample with bare and surfactant assisted namely PEG, CTAB and SHMP assisted SnO<sub>2</sub> NPs, respectively. The  $E_g$  of SnO<sub>2</sub> NPs is found to be higher than the bulk SnO<sub>2</sub> (3.6 eV) and their absorption edges showed a blue shift with a decrease in particle size and it is shown in Fig. 10b–d. This apparent blue shift of the band gap represents the position dependent quantum effect of the NPs.

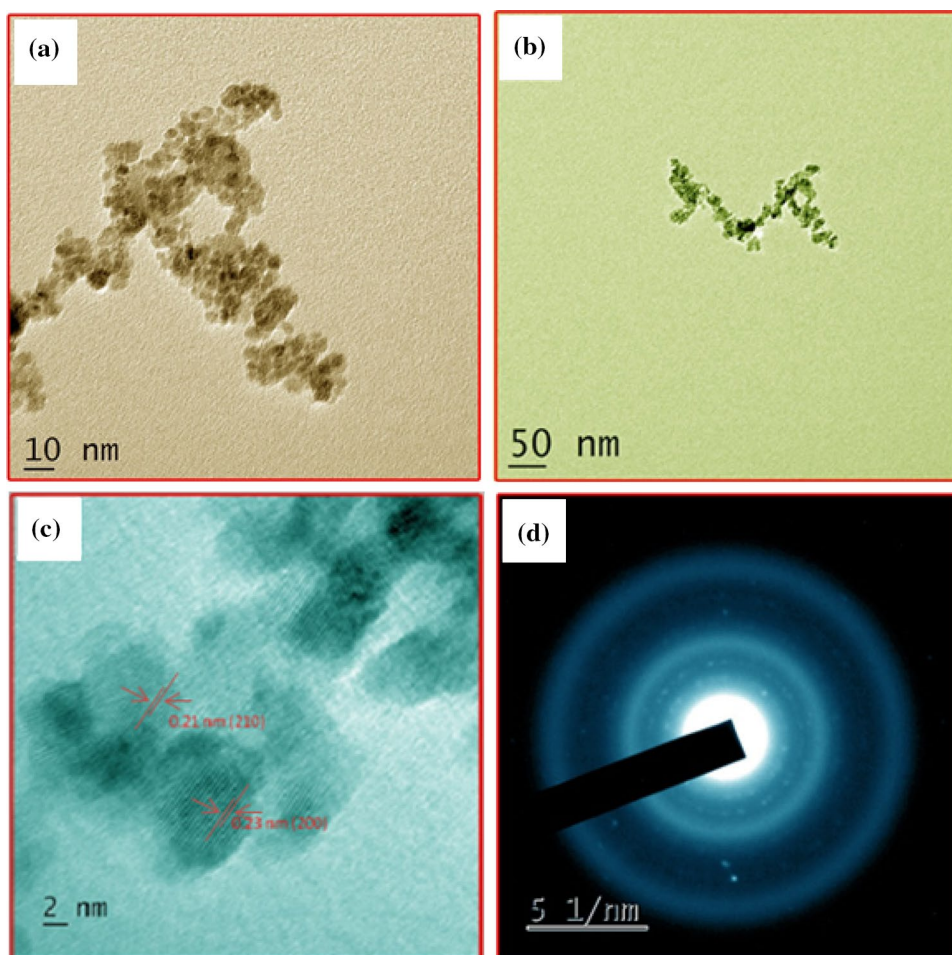
### 3.6 Photoluminescence

Photoluminescence study is important to investigate the structural defects such as oxygen vacancies, impurity and charge carrier interaction. Figure 11 depicts the PL spectra of both SnO<sub>2</sub> NPs. The PL spectra are recorded at the excitation wavelength at 300 nm. In general, the position and the intensity of the PL emissions are found to be strongly

surfactant dependent due to the nature of the functional group in the surfactant head group and also the strength of the surfactant–NPs interactions. As seen in Fig. 11, two UV and three visible peaks are observed at 327 nm, 386 nm, 451 nm, 467 nm, and 500 nm, respectively. The emission spectra are found to be similar for bare and all surfactant assisted SnO<sub>2</sub> NPs, with minor variation. The UV emission peak at 386 nm is assigned to the direct recombination of electron from conduction band to the holes in valance band. The visible emission peaks are observed at 451 nm, 467 nm, and 500 nm, and they cannot be assigned to direct recombination. The recombination is very important in determining the defects like oxygen and tin impurities and sometimes it is used to estimate the efficiency of charge transfer within the material system. Further, the green emission observed at 500 nm is attributed to the presence of oxygen vacancies in the synthesized SnO<sub>2</sub> NPs. The photoluminescence intensity of SHMP assisted SnO<sub>2</sub> NPs are found to be lower than that of bare and other surfactant assisted SnO<sub>2</sub> NPs. This specifies as PL restricts electron hole radiative recombination. Due to this it has longer life time of the photogenerated carriers. Further, these results will favor the increased



**Fig. 7** **a** and **b** TEM images of synthesized SHMP assisted SnO<sub>2</sub> nanoparticles, **c** HRTEM images of synthesized SHMP assisted SnO<sub>2</sub> nanoparticles and **d** SAED pattern of synthesized SHMP assisted SnO<sub>2</sub> nanoparticles



photocatalytic activity [62]. Therefore, in the present work, the SHMP assisted SnO<sub>2</sub> NPs are mainly studied for the applications of photocatalytic activity and electrochemical performance.

### 3.7 Evaluation of the photocatalytic activity of synthesized bare SnO<sub>2</sub> and surfactant (SHMP) assisted SnO<sub>2</sub> NPs

Methyl violet (MV) dye is a water-soluble dye which is used in textile industries, paper dyeing, paints, and biomedical field. MV may cause severe skin and eye irritation. If MV is inhaled the respiratory tract and the gastrointestinal tract will be damaged. Hence, dye removal is of enormous value. In the present work, methyl violet dye is chosen for evaluating the photocatalytic activity of SnO<sub>2</sub> NPs. Figure 12a represents the absorption spectra of an aqueous MV solution in the absence of catalyst under the sunlight irradiation. The experimental data shows the degradation rate of MV is about 13% after 120 min, as shown in Fig. 14. The result shows that MV in aqueous solution is degraded sparingly under sunlight irradiation without the catalyst. The MV has

a strong absorption peak at 573 nm, and this peak position is chosen to monitor the photocatalytic degradation process. Figure 12b shows photocatalytic experiments are carried out in the presence of bare SnO<sub>2</sub>. Figure 12c exhibits SHMP assisted SnO<sub>2</sub> catalyst on the photodegradation of MV in aqueous solution under sunlight irradiation. The absorption band of MV solution at 573 nm indicate a steady increase with increase of light irradiation time. The strong absorption band completely disappears after 120 min, which indicates the complete decomposition of MV from violet to colorless.

The investigations are also performed using SHMP assisted SnO<sub>2</sub> as a photocatalyst for the photodegradation of MV under the sunlight irradiation. The absorption spectra of photocatalytic degradation of MV dye using SHMP assisted SnO<sub>2</sub> NPs under direct sunlight is depicted in Fig. 12c. The absorption spectra of the dye (MV) show a strong absorption band around 573 nm. As SHMP assisted SnO<sub>2</sub> NPs are added the absorption band is decreased when irradiation time is increased. The strong absorption band is disappeared within 120 min and the color of the MV solution also faded away. This result indicates the complete destruction of the MV dye.

**Fig. 8** The size distribution histograms in SnO<sub>2</sub> nanoparticles **a** Bare, **b** PEG assisted, **c** CTAB assisted and **d** SHMP assisted

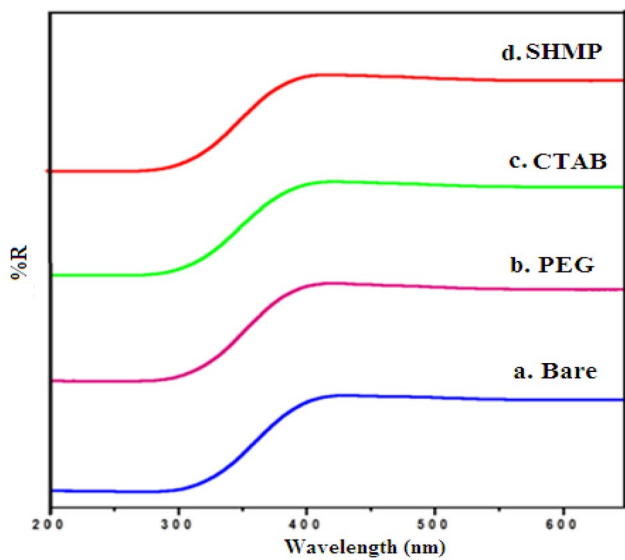
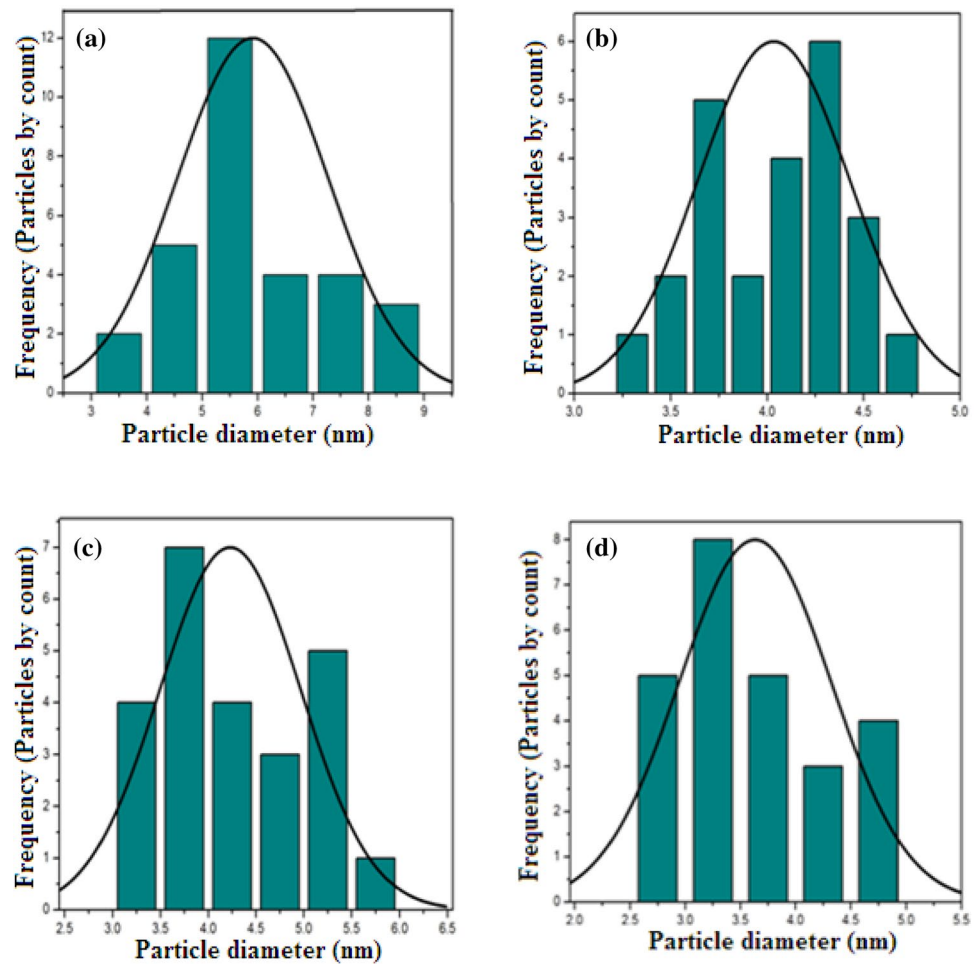


**Fig. 9** UV-Vis diffuses reflectance spectra of synthesized SnO<sub>2</sub> nanoparticles **a** Bare, **b** PEG assisted, **c** CTAB assisted and **d** SHMP assisted

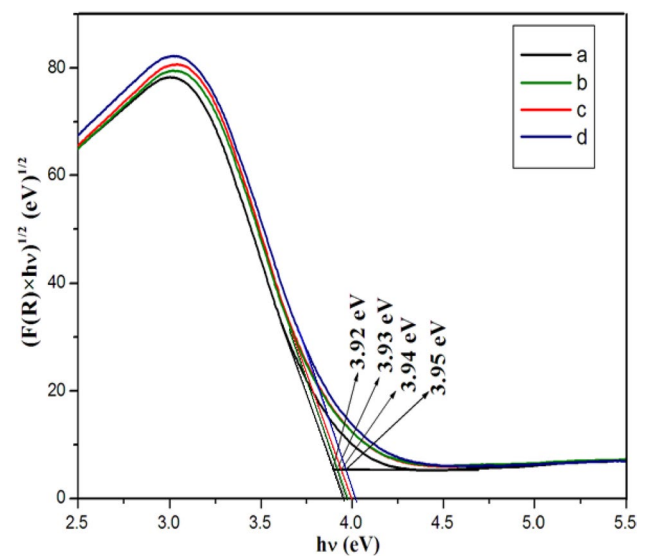


**Fig. 10** Plot of direct band gap energy for synthesized sample **a** Bare, **b** PEG assisted, **c** CTAB assisted and **d** SHMP assisted

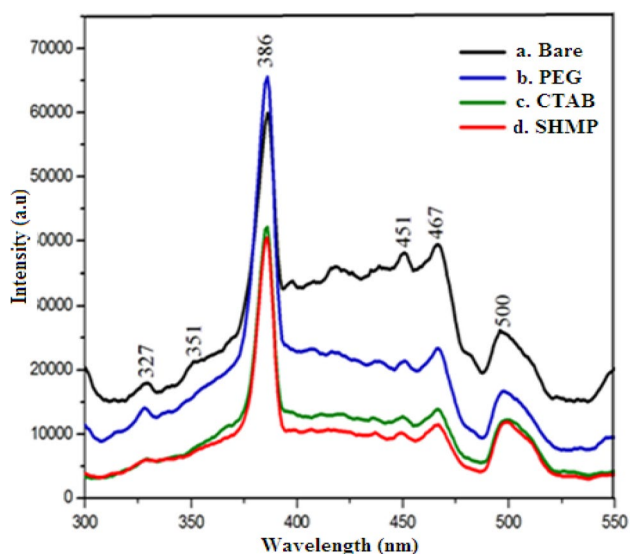


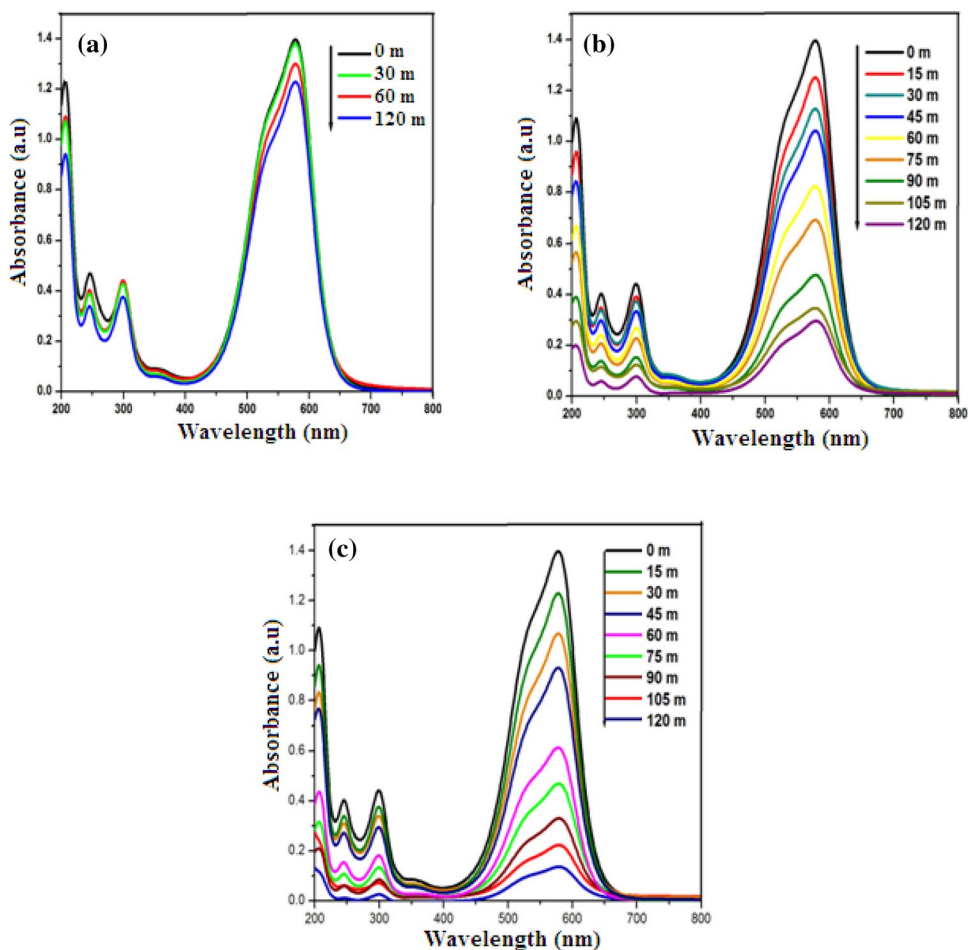
**Fig. 11** PL spectra of synthesized SnO<sub>2</sub> nanoparticles a Bare, b PEG assisted, c CTAB assisted and d SHMP assisted

It has been proved that the degradation of MV dye follows Pseudo-first order reaction and its kinetics can be determined by the following expression [63],

$$\ln\left(\frac{C_0}{C}\right) = Kt \quad (6)$$

where  $K$  is the apparent first-order rate constant,  $C_0$  is the concentration of before degradation of dye and  $C$  is the concentration of after degradation of dye. Figure 13 depicted the plot of  $\ln\left(\frac{C_0}{C}\right)$  versus irradiation time ( $t$ ) for photodegradation of MV dye using synthesized bare SnO<sub>2</sub> NPs and SHMP assisted SnO<sub>2</sub> NPs. The plot gives a linear relationship between  $\ln\left(\frac{C_0}{C}\right)$  and time. The rate constant was calculated from the slope of the plot of  $\ln\left(\frac{C_0}{C}\right)$  versus time. The values of rate constants are found to be  $0.01364 \text{ min}^{-1}$  and  $0.01962 \text{ min}^{-1}$  for bare and SHMP assisted SnO<sub>2</sub> NPs, respectively. The increased  $K$  values suggest the improved photocatalytic activity of SHMP assisted SnO<sub>2</sub> NPs. The photodegradation percentage of MV dye in the presence of bare and SHMP assisted SnO<sub>2</sub> NPs can be calculated from the following equation [64].

**Fig. 12** a UV-Vis absorption spectra of MV at different times in the absence of catalyst, b UV-Vis absorption spectra of MV at different times in the presence of the bare SnO<sub>2</sub> catalyst, c UV-Vis absorption spectra of MV at different times in the presence of the SHMP assisted SnO<sub>2</sub> catalyst



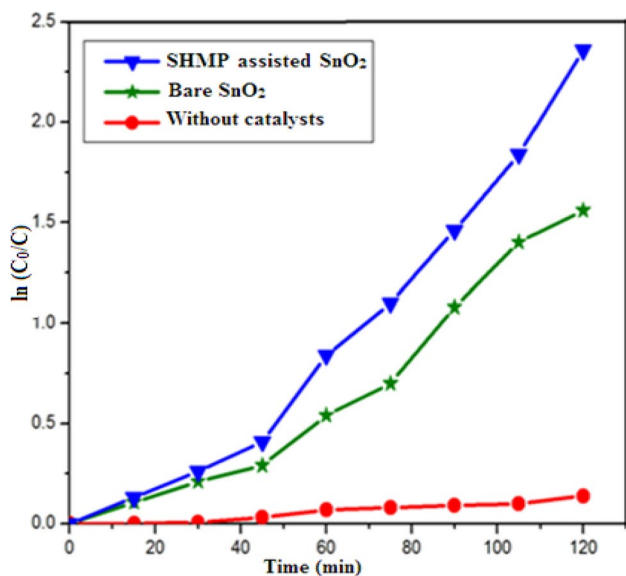


**Fig. 13** Pseudo-first-order reaction kinetic linear relationship curves for different photocatalysts

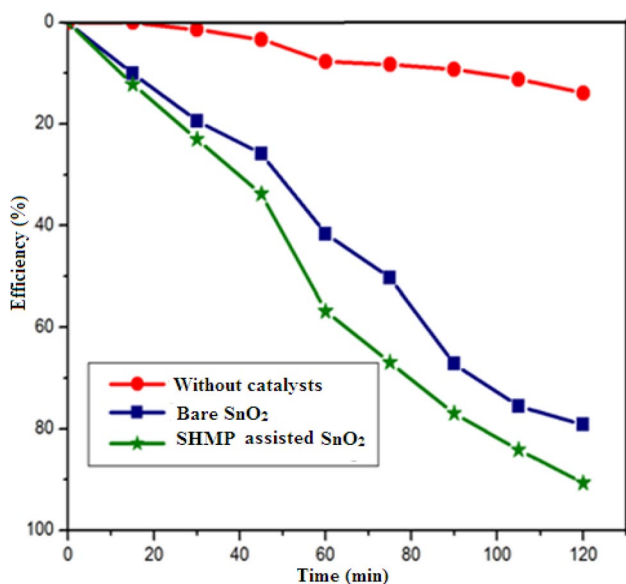


**Fig. 14** Percentage of photocatalytic degradation curves for different photocatalysts

$$X = \left[ \frac{C_0 - C_t}{C_0} \right] \times 100 \tag{7}$$

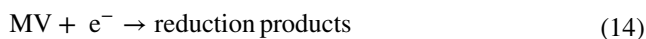
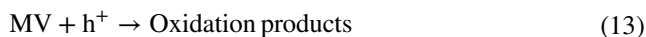
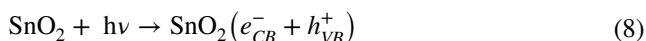
where  $C_0$  is the initial concentration of the dye and  $C_t$  is the concentration of dye after irradiation in selected time interval. The percentage efficiency for photodegradation of MV dye was displayed graphically in Fig. 14. From the graph, it is observed that 80% of the dye degraded photochemically within 120 min under direct sunlight using  $\text{SnO}_2$  NPs and

about 90% of MV degraded within 120 min under direct sunlight using SHMP assisted  $\text{SnO}_2$  NPs. In the presence of sunlight from the aqueous solution the MV dye is photodegraded and this indicates that the SHMP assisted  $\text{SnO}_2$  NPs have higher efficiency compare to bare  $\text{SnO}_2$  NPs. The enhanced photocatalytic activity may be due to the fact that SHMP assisted  $\text{SnO}_2$  NPs have a greater uniformity in particle size distribution, lower PL intensity and the inhibition of electron–hole recombination. Moreover, the uniform smaller size and well dispersed spherical shape of SHMP assisted  $\text{SnO}_2$  photocatalyst also favors the transfer of both electrons and holes generated inside the crystal lattice and facilitates the degradation of MV solutions.

### 3.8 Mechanism of photodegradation of MV using synthesised $\text{SnO}_2$ NPs

The detailed mechanism of photocatalysis can be discussed as follows: When the surface of  $\text{SnO}_2$  NPs is irradiated with sunlight,  $\text{SnO}_2$  NPs absorb the light photons. As the absorbed photon of energy is greater than its band gap energy of  $\text{SnO}_2$ , electrons ( $e^-$ ) are excited from the valence band to the conduction band, electrons-hole pairs are generated. The formation of holes ( $h^+$ ) stay in the valence band and electron ( $e^-$ ) stay in the conduction band (Eq. 8). The holes ( $h^+$ ) act as an oxidizing agent, and react with the pollutant directly (or) with hydroxyl groups and water molecules to produce hydroxyl radicals ( $\text{OH}^\cdot$ ), (Eqs. 9, 10). This is an extremely strong oxidizing agent for complete decomposition of MV molecules. The electron ( $e^-$ ) reacts on the oxygen as a reducing agent to produce superoxide radical anion ( $\text{O}_2^-$ ) (Eq. 11). The mechanisms for the photocatalytic degradation of dye molecules under the sunlight irradiation are summarized in (Eqs. 12–14).

The degradation mechanism of MV on  $\text{SnO}_2$  nanocatalyst is as follows [51].



### 3.9 Cyclic voltammetry study (CV)

To investigate the electrochemical performance of the bare  $\text{SnO}_2$  and SHMP assisted  $\text{SnO}_2$  electrodes, cyclic

voltammetry experiment is performed within the potential range from -0.4 to 0.4 V at different scan rates of 5, 10, 20 and 50  $\text{mVs}^{-1}$ . In this work, the  $\text{SnO}_2$  electrode was performed in 6 M KOH electrolyte.

Figures 15 and 16 depict the CV curve of bare and SHMP assisted  $\text{SnO}_2$  NPs. The CV curves of these both NPs display a quasi-rectangular shape without any obvious redox peaks, which indicate the ideal EDLC behavior. With the increase in scan rates, CV curves of bare and SHMP assisted NPs still maintain the nearly rectangular shapes demonstrating a favorable high-rate performance. The scan rate is increased from 5 to 50  $\text{mVs}^{-1}$ , the shape of the CV curve shows a little evaluation which indicate the good kinetic electrochemical reversibility and it is seen in Figs. 15 and 16. The specific capacitance of both electrodes (bare  $\text{SnO}_2$  and SHMP assisted  $\text{SnO}_2$ ) is calculated from the CV curves according to the following equation [65].

$$C_s = \frac{Q}{\Delta V m} \quad (15)$$

where  $C_s$  is the specific capacitance,  $Q$  is the anodic and cathodic charges on each scanning,  $m$  is the mass of the active material (mg) in the electrode and  $\Delta V$  is the scan rate ( $\text{mVs}^{-1}$ ). Based on the above equation, the bare  $\text{SnO}_2$  electrode exhibit the specific capacitance of 87, 81, 78 and 71  $\text{Fg}^{-1}$ , respectively for different scan rates 5, 10, 20 and 50  $\text{mVs}^{-1}$ , whereas the SHMP assisted  $\text{SnO}_2$  electrode exhibit the specific capacitance of 115, 103, 96 and 80  $\text{Fg}^{-1}$ , respectively for different scan rates 5, 10, 20 and 50  $\text{mVs}^{-1}$ . It is obvious that the scan rate from increases 5  $\text{mVs}^{-1}$  to 50  $\text{mVs}^{-1}$ , the specific capacitance of all the electrode material decreases, which is attributed to the diffusion effect. The

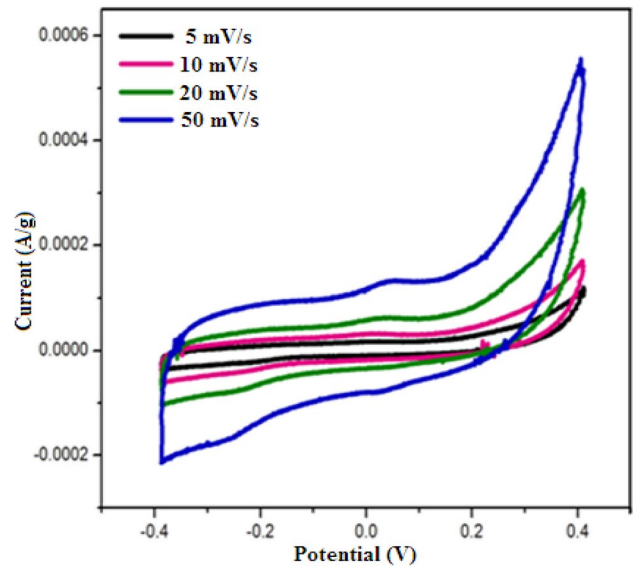


Fig. 16 CV curve of SHMP assisted  $\text{SnO}_2$  at different scan rates

specific capacitances is calculated from the CV curve and the graph is drawn between capacitance and scan rate (Fig. 17). The highest specific capacitance 115  $\text{Fg}^{-1}$  is observed for SHMP assisted  $\text{SnO}_2$  at 5  $\text{mVs}^{-1}$  scan rate, whereas at the same scan rate the bare  $\text{SnO}_2$  has a maximum specific capacitance of 87  $\text{Fg}^{-1}$ , which is lower than that of the SHMP assisted  $\text{SnO}_2$  electrode. As the scan rate increases from 5 to 50  $\text{mVs}^{-1}$ , the specific capacity of both electrode material (bare and SHMP assisted  $\text{SnO}_2$ ) decreases. The reduction in the capacity at higher scan rates is assisted to the ion exchange mechanism. At the lower scan rates, electrolyte

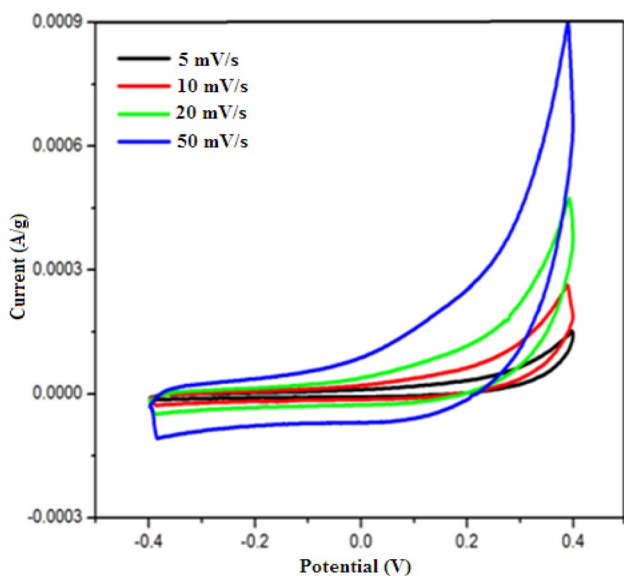


Fig. 15 CV curve of bare  $\text{SnO}_2$  at different scan rates

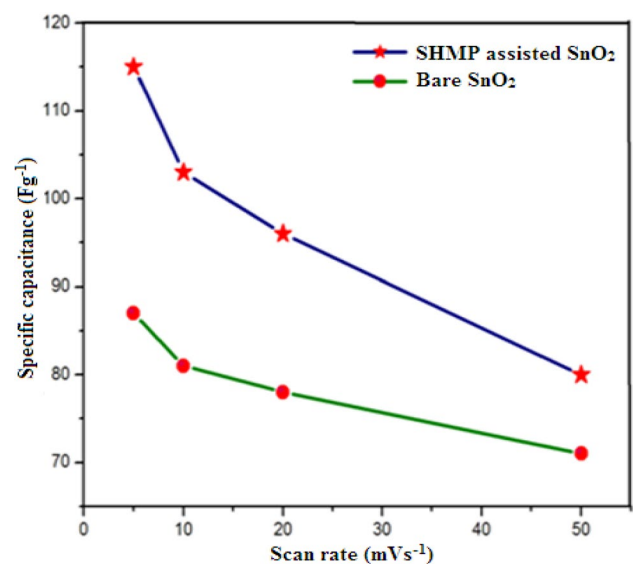


Fig. 17 Variations of specific capacitances at different scan rates

ions find sufficient time to intercalate/deintercalate with the interior (active sites) of the electrode material, but at higher scan rates, the electrolyte ions could intercalate/deintercalate mostly on the surface.

### 3.10 Galvanostatic charge–discharge studies (GCD)

Figures 18 and 19 depict the galvanostatic charge–discharge curve of bare and SHMP assisted  $\text{SnO}_2$  NPs, at different current densities of 0.05, 0.1, 0.2 and  $0.3 \text{ Ag}^{-1}$ , within the potential range between  $-0.4 \text{ V}$  and  $0.4 \text{ V}$ . The galvanostatic charge–discharge curves are recorded in the potential range selected from the CV curve. The specific capacitance ( $C_s$ ) of the electrode can be calculated using the following equation [65].

$$C_s = \frac{i\Delta t}{\Delta V m} \quad (16)$$

where  $\Delta t$  is the discharge time,  $i$  is the discharge current,  $\Delta V$  is the potential change during the discharge and  $m$  represents the mass of active material in  $\text{SnO}_2$  electrode. The specific capacitance values of the  $\text{SnO}_2$  electrode obtained from the discharge curves are 69, 54, 46 and  $26 \text{ Fg}^{-1}$  at the current densities of 0.05, 0.1, 0.2 and  $0.3 \text{ Ag}^{-1}$ , respectively (Fig. 20). Further, the specific capacitance values of the SHMP assisted  $\text{SnO}_2$  electrode obtained from the discharge curves are 98, 81, 72 and  $65 \text{ Fg}^{-1}$  at the current densities of 0.05, 0.1, 0.2 and  $0.3 \text{ Ag}^{-1}$ , respectively. In both electrodes (bare and SHMP assisted  $\text{SnO}_2$ ), all the current densities are found to be increased but specific capacitance is decreased. As the current densities are increased from 0.05 to  $0.3 \text{ Ag}^{-1}$ ,

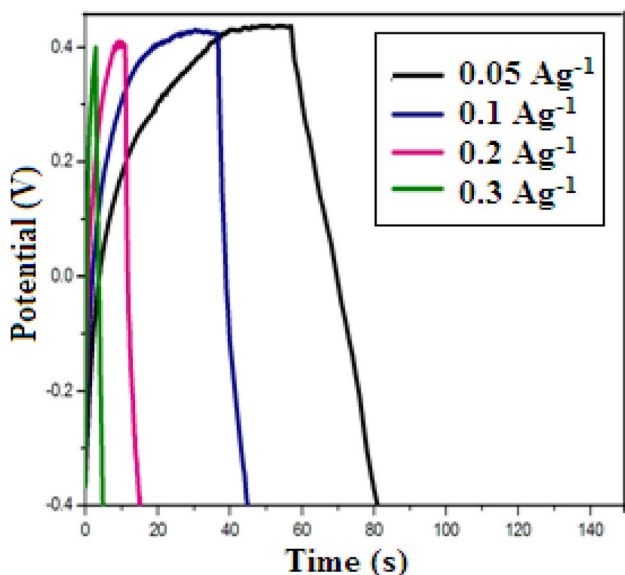


**Fig. 18** Galvanostatic charging/discharging curves of bare  $\text{SnO}_2$  at different current densities

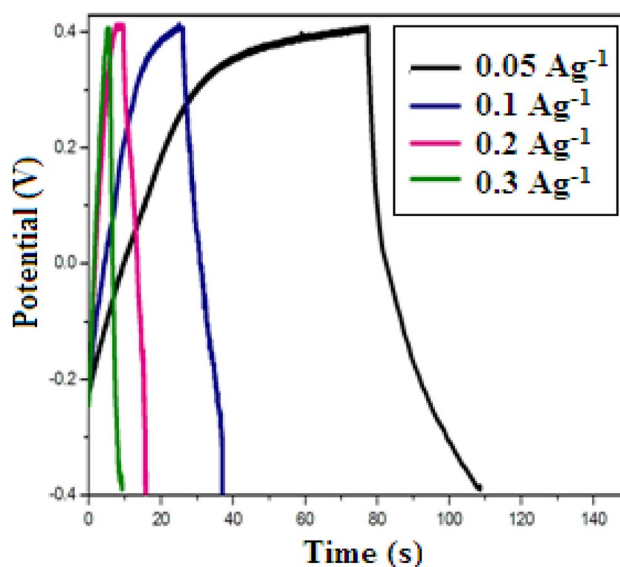


**Fig. 19** Galvanostatic charging/discharging curves of SHMP assisted  $\text{SnO}_2$  at different current densities

the specific capacitance values are decreased owing to the limited movement of electrolyte ions through the electrode material. At lower current density, the higher specific capacitance of SHMP assisted  $\text{SnO}_2$  is obtained which is superior than bare  $\text{SnO}_2$  electrode. These results indicate the sufficient transfer time for ions between the electrolyte and the electrode.

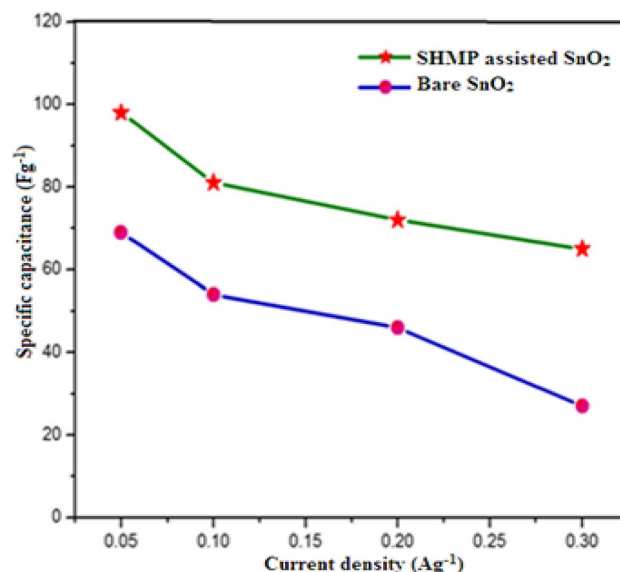
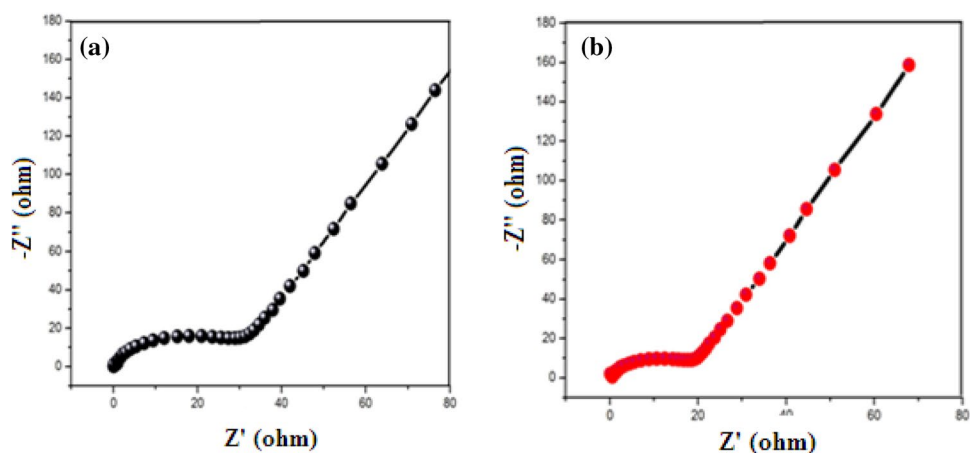


**Fig. 20** Variations of specific capacitances at different current densities

**Fig. 21** Nyquist plot obtained for **a** Bare SnO<sub>2</sub> and **b** SHMP assisted SnO<sub>2</sub>



### 3.11 Electrochemical impedance analysis (EIS)

The EIS is performed to investigate the electrochemical behavior of the bare and SHMP assisted SnO<sub>2</sub> electrode materials. The impedance of both electrodes are measured in the frequency range 100 kHz to 0.1 Hz. Nyquist plots of bare SnO<sub>2</sub> and SHMP assisted SnO<sub>2</sub> electrodes are shown in Fig. 21a, b. Partial semicircle in the high frequency region and a straight line in the low-frequency region is seen in the plots. The high frequency arc is related to the charge transfer resistance (R<sub>ct</sub>) between the electroactive material and electrolyte interface. At 45° angle with the real axis, the Warburg line is obtained at low frequency region and it is a result of the frequency dependence of ion diffusion at the electrolyte–electrode interface. This line is parallel to the imaginary axis indicating an ideal behavior. It represents the ion diffusion in the structure of the electrode materials. After adding SHMP, the conductivity of the electrode is increased, and therefore the radius of the semicircle is decreased, and a smaller semicircle means smaller charge transfer resistance. In the low-frequency region, the impedance plot of SHMP assisted SnO<sub>2</sub> electrode exhibits a nearly straight line of a limiting diffusion process, which is a characteristic feature of pure capacitive behavior. The EIS results suggest that the capacitive behavior of SHMP assisted SnO<sub>2</sub> is better than bare SnO<sub>2</sub>.

## 4 Conclusions

Bare and surfactant assisted SnO<sub>2</sub> NPs were synthesized by a facile and cost effective hydrothermal method. The XRD and SAED patterns of SnO<sub>2</sub> NPs revealed the tetragonal structure. From the TEM and HRSEM it is apparent that the bare, PEG, CTAB and SHMP assisted SnO<sub>2</sub> NPs are spherical, with an average particle size of 5.3, 4.44, 4.31 and 3.33 nm respectively. The particle size obtained from the TEM images are also in good agreement with XRD pattern.

The band gap energy of synthesized bare, PEG, CTAB, and SHMP assisted SnO<sub>2</sub> NPs are found to be 3.92, 3.93, 3.94 and 3.95 eV, respectively. The particle size decreased from 5.3 nm to 3.33 nm. For the SHMP assisted SnO<sub>2</sub> NPs the PL spectra reflected the suppression of the recombination of the photogenerated carriers. For the photodegradation of MV under direct sunlight irradiation from 0 to 120 min, the SHMP assisted SnO<sub>2</sub> NPs revealed better photocatalytic activity as compared to bare SnO<sub>2</sub>. The electrochemical performance of the SHMP assisted SnO<sub>2</sub> electrode reached a maximum of specific capacitance up to 115 Fg<sup>-1</sup>. Hence, it is suggested that bare and SHMP assisted SnO<sub>2</sub> are suitable as electrode material for supercapacitor applications.

## References

1. R. Barik, N. Devi, V.K. Perla, S.K. Ghosh, K. Mallick, Stannous sulphide nanoparticles for supercapacitor application. *Appl. Surf. Sci.* **472**, 112–117 (2019)
2. A.A. Ali, A.A. Nazeer, M. Madkour, A. Bumajdad, F.A. Sagheer, Novel supercapacitor electrodes based semiconductor nanoheterostructure of CdS/rGO/CeO<sub>2</sub> as efficient candidates. *Arab. J. Chem.* **11**(5), 692–699 (2018)
3. J.P. Zheng, T.R. Jow, High energy and high power density electrochemical capacitors. *J. Power Sour.* **62**(2), 155–159 (1996)
4. L. Mai, X. Tian, X. Xu, L. Chang, L. Xu, Nanowire electrodes for electrochemical energy storage devices. *Chem. Rev.* **114**(23), 11828–11862 (2014)
5. H. Chen, M. Ling, L. Hencz, H.Y. Ling, G. Li, Z. Lin, G. Liu, S. Zhang, Exploring chemical, mechanical, and electrical functionalities of binders for advanced energy-storage devices. *Chem. Rev.* **118**(18), 8936–8982 (2018)
6. J. Xiao, Q.L. Wu, P. Liu, Y. Liang, H.B. Li, M.M. Wu, G.W. Yang, Highly stable sub-5 nm Sn<sub>6</sub>O<sub>4</sub>(OH)<sub>4</sub> nanocrystals with ultrahigh activity as advanced photocatalytic materials for photodegradation of methyl orange. *Nanotechnology* **25**, 135702 (2014)
7. S.P. Kim, M.Y. Choi, H.C. Choi, Photocatalytic activity of SnO<sub>2</sub> nanoparticles in methylene blue degradation. *Mater. Res. Bull.* **74**, 85–89 (2016)
8. G. Durai, M. Rajasimman, Biological treatment of tannery wastewater—a review. *J. Environ. Sci. Technol.* **4**(1), 1–17 (2011)

9. S. Niu, Y. Wang, S. Lu, D. Wang, P. Wang, Fabrication and photocatalytic properties of SnO<sub>2</sub> double-shelled and triple-shelled hollow spheres. *Solid State Sci.* **56**, 63–67 (2016)
10. A. Esmaeili-Bafghi-Karimabad, D. Ghanbari, M. Salavati-Niasari, L. Nejati-Moghadam, S. Gholamrezaei, Photo-catalyst tin dioxide: synthesis and characterization different morphologies of SnO<sub>2</sub> nanostructures and nanocomposites. *J. Mater. Sci.* **26**(9), 6970–6978 (2015)
11. Y. Yu, S. Qu, D. Zang, L. Wang, H. Wu, Fast synthesis of Pt nanocrystals and Pt/microporous La<sub>2</sub>O<sub>3</sub> materials using acoustic levitation. *Nanoscale Res. Lett.* **13**, 50 (2018)
12. S. Qu, Y. Yu, K. Lin, P. Liu, C. Zheng, L. Wang, T. Xu, Z. Wan, H. Wu, Easy hydrothermal synthesis of multi-shelled La<sub>2</sub>O<sub>3</sub> hollow spheres for lithium-ion batteries. *J. Mater. Sci.* **29**(2), 1232–1237 (2018)
13. Z. Jia, D. Lan, K. Lin, M. Qin, K. Kou, G. Wu, H. Wu, Progress in low-frequency microwave absorbing materials. *J. Mater. Sci.* **29**(20), 17122–17136 (2018)
14. H. Wu, G. Wu, Y. Ren, L. Yang, L. Wang, X. Li, Co<sup>2+</sup>/Co<sup>3+</sup> ratio dependence of electromagnetic wave absorption in hierarchical NiCo<sub>2</sub>O<sub>4</sub>-CoNiO<sub>2</sub> hybrids. *J. Mater. Chem. C* **3**, 7677–7690 (2015)
15. Z. Jia, K. Lin, G. Wu, H. Xing, H. Wu, Recent progresses of high-temperature microwave-absorbing materials. *NANO* **13**(6), 1830005 (2018)
16. H. Wu, G. Wu, Y. Ren, X. Li, L. Wang, Multishelled metal oxide hollow spheres: easy synthesis and formation mechanism. *Chem. Eur. J.* **22**, 8864–8871 (2016)
17. H. Wu, G. Wu, L. Wang, Peculiar porous  $\alpha$ -Fe<sub>2</sub>O<sub>3</sub>,  $\gamma$ -Fe<sub>2</sub>O<sub>3</sub> and Fe<sub>3</sub>O<sub>4</sub> nanospheres: facile synthesis and electromagnetic properties. *Powder Technol.* **269**, 443–451 (2015)
18. Z.R. Jia, Z.G. Gao, D. Lan, Y.H. Cheng, G.L. Wu, H.J. Wu, Effects of filler loading and surface modification on electrical and thermal properties of epoxy/montmorillonite composite. *Chin. Phys. B* **27**(11), 117806 (2018)
19. D. Lan, M. Qin, R. Yang, S. Chen, H. Wu, Y. Fan, Q. Fu, F. Zhang, Facile synthesis of hierarchical chrysanthemum-like copper cobaltate-copper oxide composites for enhanced microwave absorption performance. *J. Colloid Interface Sci.* **533**, 481–491 (2019)
20. H. Wu, S. Qu, K. Lin, Y. Qing, L. Wang, Y. Fan, Q. Fu, F. Zhang, Enhanced low-frequency microwave absorbing property of SCFs@TiO<sub>2</sub> composite. *Powder Technol.* **333**, 153–159 (2018)
21. L. Xiao, W. Sun, X. Zhou, Z. Cai, F. Hu, Facile synthesis of mesoporous MnO<sub>2</sub> nanosheet and microflower with efficient photocatalytic activities for organic dyes. *Vacuum* **156**, 291–297 (2018)
22. X. Li, C. Hu, X. Wang, Y. Xi, Photocatalytic activity of CdS nanoparticles synthesized by a facile composite molten salt method. *Appl. Surf. Sci.* **258**(10), 4370–4376 (2012)
23. B.G.S. Raj, A.M. Asiri, A.H. Qusti, J.J. Wu, S. Anandan, Sonochemically synthesized MnO<sub>2</sub> nanoparticles as electrode material for supercapacitors. *Ultrason. Sonochem.* **21**(6), 1933–1938 (2014)
24. S. Sagadevan, Z.Z. Chowdhury, M.R.B. Johan, F.A. Aziz, L.S. Roselin, H.L. Hsu, R. Selvin, Synthesis characterization and electrochemical properties of cadmium sulfide-reduced graphene oxide nanocomposites. *Results Phys.* **12**, 878–885 (2019)
25. R.M. Kore, B.J. Lokhande, A robust solvent deficient route synthesis of mesoporous Fe<sub>2</sub>O<sub>3</sub> nanoparticles as supercapacitor electrode material with improved capacitive performance. *J. Alloys Compd.* **725**, 129–138 (2017)
26. G.V. Pereira, V.A. Freitas, H.S. Oliveira, L.C.A. Oliveira, J.C. Belchior, A photocatalytic process for the eradication of dengue through •OH generation in the presence of sunlight and iron oxide. *RSC Adv.* **4**, 63650–63654 (2014)
27. M. Jayalakshmi, M. MohanRao, N. Venugopal, Kwang-Bum-Kim, Hydrothermal synthesis of SnO<sub>2</sub>-V<sub>2</sub>O<sub>5</sub> mixed oxide and electrochemical screening of carbon nano-tubes (CNT), V<sub>2</sub>O<sub>5</sub>, V<sub>2</sub>O<sub>5</sub>-CNT, and SnO<sub>2</sub>-V<sub>2</sub>O<sub>5</sub>-CNT electrodes for supercapacitor applications. *J. Power Sour.* **166**(2), 578–583 (2007)
28. M. Shanmugam, A. Alsalmeh, A. Alghamdi, R. Jayavel, Enhanced photocatalytic performance of Graphene-V<sub>2</sub>O<sub>5</sub> nano-composite in the degradation of methylene blue dye under direct sunlight. *ACS Appl. Mater. Interfaces.* **7**(27), 14905–14911 (2015)
29. M. Wu, W. Zeng, Q. He, J. Zhang, Hydrothermal synthesis of SnO<sub>2</sub> nanocorals, nanofragments and nanograss and their formaldehyde gas-sensing properties. *Mater. Sci. Semicond. Process.* **16**, 1495–1501 (2013)
30. B.M. Matin, Y. Mortazavi, A.A. Khodadadi, A. Abbasia, A.A. Firooz, Alkaline- and template-free hydrothermal synthesis of stable SnO<sub>2</sub> nanoparticles and nanorods for CO and ethanol gas sensing. *Sens. Actuators, B* **151**, 140–145 (2010)
31. E. Ramasamy, J. Lee, Ordered mesoporous SnO<sub>2</sub>-based photoanodes for high-performance dye-sensitized solar cells. *J. Phys. Chem. C* **114**, 22032–22037 (2010)
32. Y. Yang, X. Zhao, H.E. Wang, M. Li, C. Hao, M. Ji, S. Ren, G. Cao, Phosphorized SnO<sub>2</sub>/Graphene heterostructure for highly reversible lithium-ion storage with enhanced pseudocapacitance. *J. Mater. Chem. A.* **6**, 3479–3487 (2018)
33. Y. Sun, W.D. Chemelewski, S.P. Berglund, C. Li, H. He, G. Shi, C.B. Mullins, Antimony-doped tin oxide nanorods as a transparent conducting electrode for enhancing photoelectrochemical oxidation of water by hematite. *Appl. Mater. Interfaces* **6**, 5494–5499 (2014)
34. L.C. Nehru, V. Swaminathan, C. Sanjeeviraja, Photoluminescence studies on nanocrystalline tin oxide powder for optoelectronic devices. *Am. J. Mater. Sci.* **2**(2), 6–10 (2012)
35. N. Talebian, F. Jafarinezhad, Morphology-controlled synthesis of SnO<sub>2</sub> nanostructures using hydrothermal method and their photocatalytic applications. *Ceram. Int.* **39**(7), 8311–8317 (2013)
36. B. Jia, W. Jia, F. Qu, X. Wu, General strategy for self assembly of mesoporous SnO<sub>2</sub> nanospheres and their applications in water purification. *RSC Adv.* **3**, 12140–12148 (2013)
37. M. Zhao, Q. Zhao, J. Qiu, H. Xue, Huan Pang, Tin-based nanomaterials for electrochemical energy storage. *RSC Adv.* **6**, 95449–95468 (2016)
38. A.P. Gaikwad, S.H. Patil, K.R. Patil, S.D. Sathaye, C.V. Rode, Composite thin film of simultaneously formed carbon and SnO<sub>2</sub> QDs for supercapacitance application. *New J. Chem.* **42**, 8823–8830 (2018)
39. Z. He, J. Zhou, Synthesis, characterization and activity of tin oxide nanoparticles: influence of solvothermal time on photocatalytic degradation of rhodamine B. *Mod. Res. Catal.* **2**, 13–18 (2013)
40. T.T. Bhosale, H.M. Shinde, N.L. Gavade, S.B. Babar, V.V. Gawade, S.R. Sabale, R.J. Kamble, B.S. Shirke, K.M. Garadkar, Biosynthesis of SnO<sub>2</sub> nanoparticles by aqueous leaf extract of *calotropis gigantea* for photocatalytic applications. *J. Mater. Sci.: Mater. Electron.* **29**, 6826–6834 (2018)
41. K. Bouras, J.L. Rehspringer, G. Schmerber, H. Rinnert, S. Colis, G. Ferblantier, M. Balestrieri, D. Ihiawakrim, A. Dinia, A. Slaoui, Optical and structural properties of Nd doped SnO<sub>2</sub> powder fabricated by the sol-gel method. *J. Mater. Chem. C* **2**, 8235–8243 (2014)
42. A. Kumar, L. Rout, R.S. Dhaka, S.L. Samal, P. Dash, Design of graphene oxide-SnO<sub>2</sub> nanocomposite with superior catalytic efficiency for the synthesis of  $\beta$ -enaminones and  $\beta$ -enaminoesters. *RSC Adv.* **5**, 39193–39204 (2015)
43. W.W. Wang, Y.J. Zhu, L.X. Yang, ZnO-SnO<sub>2</sub> hollow spheres and hierarchical nanosheets: hydrothermal preparation, formation mechanism and photocatalytic properties. *Adv. Funct. Mater.* **17**, 59–64 (2007)



44. M. Zhang, G. Sheng, J. Fu, T. An, X. Wang, X. Hu, Novel preparation of nanosized ZnO–SnO<sub>2</sub> with high photocatalytic activity by homogeneous co-precipitation method. *Mater. Lett.* **59**, 3641–3644 (2005)
45. Y.C. Zhang, Z.N. Du, M. Zhang, Hydrothermal synthesis of SnO<sub>2</sub>/SnS<sub>2</sub> nanocomposite with high visible light-driven photocatalytic activity. *Mater. Lett.* **65**, 2891–2894 (2011)
46. G.E. Patil, D.D. Kajale, V.B. Gaikwad, G.H. Jain, Preparation and characterization of SnO<sub>2</sub> nanoparticles by hydrothermal route. *Int. Nano Lett.* **2**, 17–21 (2012)
47. T. Mahalingam, V. Dhanasekaran, R. Chandramohan, J.K. Rhee, Microstructural properties of electrochemically synthesized ZnSe thin films. *J. Mater. Sci.* **47**, 1950–1957 (2012)
48. R.K. Mishra, P.P. Sahay, Zn-doped and undoped SnO<sub>2</sub> nanoparticles: a comparative structural, optical and LPG sensing properties study. *Mater. Res. Bull.* **47**, 4112–4118 (2012)
49. A. Arunachalam, S. Dhanapandian, C. Manoharan, M. Bououdina, G. Ramalingam, M. Rajasekaran, M. Radhakrishnan, A. Mohamedbraheem, Influence of sprayed nanocrystalline Zn-doped TiO<sub>2</sub> photoelectrode with the dye extracted from *Hibiscus Surattensis* as sensitizer in dye-sensitized solar cell. *Ceram. Int.* **42**(9), 11136–11149 (2016)
50. S. Harish, J. Archana, M. Navaneethan, A. Silambarasan, K.D. Nisha, S. Ponnusamy, C. Muthamizhchelvan, H. Ikeda, D.K. Aswal, Y. Hayakawa, Enhanced visible light induced photocatalytic activity on the degradation of organic pollutant by SnO nanoparticles decorated hierarchical ZnO nanostructures. *RSC Adv.* **6**, 89721–89731 (2016)
51. L.P. Singh, M.N. Luwang, S.K. Srivastava, Luminescence and photocatalytic studies of Sm<sup>3+</sup> ion doped SnO<sub>2</sub> nanoparticles. *New J. Chem.* **38**, 115–121 (2014)
52. V. Bonu, N. Kumar, A. Das, S. Dash, A.K. Tyagi, Enhanced lubricity of SnO<sub>2</sub> nanoparticles dispersed polyolester nanofluid. *Ind. Eng. Chem. Res.* **55**, 2696–2703 (2016)
53. E. Duraisamy, H.T. Das, A.S. Sharma, P. Elumalai, supercapacitor and photocatalytic performances of hydrothermally-derived Co<sub>3</sub>O<sub>4</sub>/CoO @ carbon nanocomposite. *New J. Chem.* **42**, 6114–6124 (2018)
54. H. Chen, L. Ding, W. Sun, Q. Jiang, J. Hu, J. Li, Synthesis and characterization of Ni doped SnO<sub>2</sub> microspheres with enhanced visible-light photocatalytic activity. *RSC Adv.* **5**, 56401–56409 (2015)
55. Y. Dong, Z. Zhao, Z. Wang, Y. Liu, X. Wang, J. Qiu, Dually fixed SnO<sub>2</sub> nanoparticles on graphene nanosheets by polyaniline coating for superior lithium storage. *ACS Appl. Mater. Interfaces.* **7**(4), 2444–2451 (2015)
56. J. Gajendiran, V. Rajendran, A study of the nano-structured aggregated tin oxides (SnO<sub>2</sub>/SnO) and their structural and photoluminescence properties by a hydrothermal method. *Mater. Lett.* **139**, 116–118 (2015)
57. B. Saravanakumar, G. Ravi, V. Ganesh, F. Ameen, A. Al-Sabri, R. Yuvakkumar, Surfactant assisted zinc doped tin oxide nanoparticles for supercapacitor applications. *J. Sol-Gel. Sci. Technol.* **86**(3), 521–535 (2018)
58. A. Bhattacharjee, M. Ahmaruzzaman, T. Sinha, Surfactant effects on the synthesis of durable tin-oxide nanoparticles and its exploitation as a recyclable catalyst for elimination of toxic dye: a green and efficient approach for wastewater treatment. *RSC Adv.* **4**, 51418–55142 (2014)
59. W. Wei, S. Gao, Z. Yang, Y. Wu, C. Chen, L. Guo, J. Li, Porous SnO<sub>2</sub> nanocubes with controllable pore volume and their Li storage performance. *RSC Adv.* **4**, 13250–13255 (2014)
60. H. Yan, P. Song, S. Zhang, Z. Yang, Q. Wang, Dispersed SnO<sub>2</sub> nanoparticles on MoS<sub>2</sub> nanosheets for superior gas-sensing performances to ethanol. *RSC Adv.* **5**, 79593–79599 (2015)
61. X. Li, B. Lin, B. Xu, Z. Chen, Q. Wang, J. Kuang, H. Zhu, Preparation and characterization of mesoporous SnO<sub>2</sub>-pillared HTaWO<sub>6</sub> with enhanced photocatalytic activity. *J. Mater. Chem.* **20**, 3924–3931 (2010)
62. B. Subash, B. Krishnakumar, R. Velmurugan, M. Swaminathan, M. Shanthi, Synthesis of Ce co-doped Ag–ZnO photocatalyst with excellent performance for NBB dye degradation under natural sunlight illumination. *Catal. Sci. Technol.* **2**, 2319–2326 (2012)
63. Y. Li, L. Zhu, Y. Guo, H. Song, Z. Lou, Z. Ye, A new type of hybrid nanostructures: complete photo-generated carriers separation and ultrahigh photocatalytic activity. *J. Mater. Chem. A* **2**, 14245–14250 (2014)
64. S.K. Jayaraj, V. Sadishkumar, T. Arun, P. Thangadurai, Enhanced photocatalytic activity of V<sub>2</sub>O<sub>5</sub> nanorods for the photodegradation of organic dyes: a detailed understanding of the mechanism and their antibacterial activity. *Mater. Sci. Semicond. Process.* **85**, 122–133 (2018)
65. K. Manikandan, S. Dhanuskodi, A.R. Thomas, N. Maheswari, G. Muralidharan, D. Sastikumar, Size-strain distribution analysis of SnO<sub>2</sub> nanoparticles and its multifunctional applications of fiber optic gas sensor supercapacitor and optical limiter. *RSC Adv.* **6**, 90559–90570 (2016)

**Publisher's Note** Springer Nature remains neutral with regard to jurisdictional claims in published maps and institutional affiliations.